

# LABORATORY DETERMINATION OF STRESS-PATH DEPENDENCY OF DIRECTIONAL PERMEABILITIES OF ESTAILLADES LIMESTONE

J. Dautriat<sup>(1,2)</sup>, N. Gland<sup>(1)</sup>, A. Dimanov<sup>(2)</sup>, J. Raphanel<sup>(2)</sup>, O. Vizika<sup>(1)</sup>

<sup>(1)</sup> Institut Français du Pétrole, 1 & 4 av. de Bois-Préau, 92852 Rueil-Malmaison, France

<sup>(2)</sup> Laboratoire de Mécanique des Solides, Ecole Polytechnique, 91128 Palaiseau, France

*This paper was prepared for presentation at the International Symposium of the Society of Core Analysts held in Abu Dhabi, UAE 29 October-2 November, 2008*

## ABSTRACT

The influence of stress paths representative of reservoir conditions on the mechanical behavior and the coupled permeability evolutions of a carbonate has been investigated. To predict the permeabilities evolutions under triaxial loading, we have developed a triaxial cell designed to allow the measurements of the permeability in three orthogonal directions, along and transverse to the maximum principal stress direction. A set of core samples are mechanically loaded following different stress paths, characterized by a constant ratio  $K=\Delta\sigma_H/\Delta\sigma_V$ . Our experimental set-up allows the monitoring of the petrophysical and geomechanical parameters during loading, before and post sample damage. The tested rock is an analog reservoir carbonate, the Estailades Limestone, characterized macroscopically by a porosity around  $\phi\sim 29\%$  and a moderate permeability around  $k\sim 150\text{ mD}$ . From our experimental results, the failure envelope of this carbonate is determined and the evolution of the directional permeabilities are examined in the  $(p',q)$  diagram. According to the followed stress path, permeabilities reductions can be limited or drastic. In addition, to identify the micro-mechanisms responsible for the measured permeabilities evolutions, we performed microstructural analyses on deformed samples. In the near-elastic domain, brittle damage induces limited directional permeabilities modifications; whereas, at higher stress, depending on  $K$ , shear induced dilation or shear induced compaction mechanisms are activated. The highest permeability drop occurred for the hydrostatic compression ( $K=1$ ), in the compaction regime, characterized by pore collapse mechanisms affecting preferentially the macroporosity.

## INTRODUCTION

Oil field production leads to change in reservoir pore pressure, resulting in modifications of effective stresses acting on the reservoir; it induces both elastic and inelastic microscale deformations and potentially compaction at the reservoir scale. The changes of the porous structure directly modify the transport properties, and thus the production efficiency (Schutjens and De Ruig, 1997). Indeed due to the reservoir boundaries conditions, the pore pressure drop affects preferentially the vertical component of stress, which has a direct

impact on the horizontal permeability, generally closely related to the production rate. It is thus of major interest to study experimentally the effects of representative stress field conditions on transport properties, and more especially the anisotropy evolutions. Whereas numerous studies of the literature are aimed at highlighting the hydro-mechanical relationships of various rock types (sandstones (Rhett and Teufel, 1992), chalks (Jones and Mathiesen, 1993), stiff carbonates (Yale and Crawford, 1998)), the common experimental set-ups are limited to the measure of the permeability evolution along the maximum principal stress direction only. In this study, samples of Estailades limestone, a high porosity and moderately permeable carbonate, have been subjected to different stress paths representative of reservoir conditions, using a triaxial cell designed to measure both the axial and radial components of the permeability tensor. Previous studies have stated that the evolutions of permeability under stress are closely related to the modification of microstructures induced by mechanical compaction effects; therefore, we complement our results for macroscopic permeability evolutions, by microstructural characterizations of the damaged samples.

## **EXPERIMENTAL PROCEDURE**

### **Experimental Set-Up**

This study has been conducted with the triaxial cell described by Dautriat et al. (2008), which is designed to allow permeability measurements in three orthogonal directions (see figure 1). The cell is operated using two high pressure pumps, in order to apply independently confining and axial pressures (ranging from 3 to 69 MPa), and one intermediate pressure pump to generate brine flows through the rock sample. To insure a constant brine viscosity in all the set-up, the cell is placed inside an oven and the pore fluid pump and the external flow lines are also thermally regulated. The cell is equipped with both radial and axial deformation sensors. The displacement of the axial piston, related to the axial shortening of the sample, is recorded by two external Linear Variable Displacement Transducers (LVDT) fastened parallel between the upper mobile piston and the lower fixed piston. The radial strains of the core are measured by a double channel cantilever sensor fastened on the sleeve inside the cell.

The most important innovation of our set-up is related to the special equipment of flow ports of the core sleeve. Usually, the permeability measurements in classical triaxial set-ups are achieved by measuring the pressure differential generated by a flow between the inlet and the outlet of a cylindrical sample in the maximal principal direction of stress. This standard measurement is still possible with our set-up (through items 8 and 9), but additionally we are able to measure the intermediate pressure differential induced by an axial fluid flow between two points located at 1cm of each sample end, using small fluid pressure samplers in contact with the lateral core surface (items 10 and 11). This original measure allows to suppress the compression end effects on axial permeability measurements, as illustrated in a previous work (Dautriat et al., 2008). In order to measure

the evolution of permeability along the diameter of the core sample, specific coaxial radial flow ports (items 12 and 13) have been installed. In two orthogonal directions, an injector is facing a receptor, to generate fluid flow and to measure the associated pressure differential. These internal flow ports are connected to the external flow lines system (item 14) by sealed feedthrus.

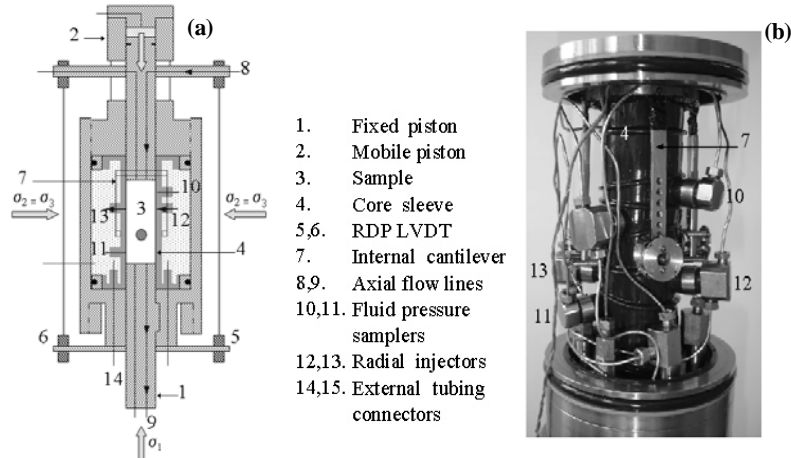


**Figure 1 :** (a) Simplified scheme of the triaxial cell used in this study and (b) picture of the equipped core sleeve, from *Dautriat et al. (2008)*.

### Permeabilities Calculation

In this study, the directional permeabilities are measured by the steady state method. The pressure differential is measured by a  $\pm 400\text{mbar}$   $\Delta p$  sensor. For stepwise loading, at least five increasing flow rates are applied. During continuous loading, a constant flow rate is used. Flows are always performed in the same directions. Both axial permeabilities are calculated using the classical Darcy equation; the differential pressure sampling length equals the sample length ( $\sim 80\text{ mm}$ ) for the case of the full-length axial permeability calculation ( $k_{az,Fl}$ ), or equals the spacing between the pressure samplers ( $\sim 60\text{ mm}$ ) for the case of mid-length axial permeability calculation ( $k_{az,ML}$ ). For the two radial measurements, a modified Darcy law is employed:

$$\frac{Q}{A_r} = G \frac{k_r}{\mu} \frac{\Delta P_p}{D},$$

where a correcting factor  $G$  is introduced to take into account the deviation from straight flow lines between the transverse flow ports of cross sections  $A_r$  along the diameter  $D$  of the sample. Following the methodology described by Bai et al. (2002) and considering the specific geometry of our set-up, a 3D finite element computation has been performed to solve the flow problem at Darcy scale and to calculate  $G$  using the relation linking the experimental flow shape to an ideal cylindrical Darcy flow:

$$G = \frac{\Delta P_{Darcy}}{\Delta P_{Exp}} = \frac{A_{Exp}}{A_{Darcy}}$$

For the ideal case of a homogeneous and isotropic material, the calculated  $G$  factor equals 5.5. This factor is quite sensitive to the permeability anisotropy of the tested materials. As discussed by Dautriat et al. (2007), the assumption of a constant value for  $G$  is valid when the transverse permeability anisotropy remains less than 20%.

### Sample Preparation

We have prepared a set of Estailades limestone samples from the same rock block oriented with an orthogonal frame (x, y, z). In order to fit the core sleeve dimensions, the cylindrical samples have a diameter  $D=38.1 \text{ mm}$  and a length  $L=80 \text{ mm}$ . All the samples have been cored along the direction  $z$  and the directions  $x$  and  $y$  have also been reported. The macroplugs are then dried at  $60 \text{ }^\circ\text{C}$  during  $48 \text{ h}$ ; their dry-weights are measured and the plugs are finally saturated under void by NaCl brine with a concentration of  $20\text{g.L}^{-1}$ ; the mass of the saturated samples are then measured in order to estimate their initial porosity. In addition, smaller samples have also been cored to perform Hg porosimetry, ultrasonic P-wave measurements and Micro Computed Tomography (MCT) scans. Finally, sample fragments were also collected for Scanning Electron Microscopy (SEM) observations.

### Compression Test Protocol

In this study, we present results obtained during moderately rated ( $\sim 6\text{MPa.h}^{-1}$ ) continuous loading. As discussed by Heiland and Raab (2001), the continuous loading (opposed to the stepwise loading) limit the effects of differed mechanisms of deformation accommodating the imposed stress, such as creep mechanism, which could influence the permeability measurements. However, by operating in continuous mode, we are not able to measure simultaneously the directional permeability evolutions on a single sample and we need to use several samples to describe the carbonate hydro-mechanical behaviour for different stress path. The saturated sample is placed vertically into the core sleeve, an initial hydrostatic pressure of  $3\text{MPa}$  is applied to ensure the sealing of the core sleeve around the sample, and the pore pressure is increased up to  $1\text{MPa}$ . The temperature of the oven is then regulated at  $40^\circ\text{C}$ , as well as the pore fluid pump and the external flow lines. When the thermal equilibrium of the system is reached ( $\sim 12\text{h}$ ); the deformation sensors are initialized to zero. At this stage, a first set of permeability measurements  $\{k_{az,FI}; k_{az,MI}; k_{rx}$  and  $k_{ry}\}$  is performed at  $3\text{MPa}$  in the three directions. During the loading, a moderate constant flow rate is applied through the sample and the induced small pressure differential is measured in the considered flow direction, at constant back pressure of  $1\text{MPa}$ . The axial loading is performed at a small rate of  $0.1\text{MPa.min}^{-1}$  and the confining pressure is increased keeping  $K=\Delta\sigma_r/\Delta\sigma_a$  constant. The experiment is stopped when a sample failure occurs or when the pressure limit of  $\sim 69\text{MPa}$  is reached. During the loading, the pressure differential evolution as well as the axial and radial deformations are recorded on an acquisition bench and stored

on a computer. The permeability can then be calculated taking into account the deformations of the sample and the direction of measurement.

### TESTED MATERIAL – PETROPHYSICAL PROPERTIES

The studied material is a natural carbonate, the Estailades limestone, obtained at the Oppède quarry in the south of France. As revealed by the MicroTomography reconstructions and the Scanning Electron Microscopy observations, this carbonate is composed of two kinds of loosely packed dense or microporous calcite aggregates. In Back Scattering Electron images, the dense and microporous calcite clusters appear in light and dark grey (see Fig. 2a) respectively, while the macroporosity (figure 1a) and the microporosity (see Fig. 2b) of the loose calcite aggregates appear in black.

The porosity of the samples has been measured using different techniques, dry-wet weight measurements, CT-Scan profiles on the macro-plugs, Nitrogen Accupic, Hg porosimetry on the microplugs. Absolute Permeability has been measured on a single flow set-up using the steady state technique as described previously. The porosity measured by dry-wet weights is close to 29 % and the average initial permeability is about 150 *mD*. The bimodal distribution of the pore radii extracted from the Hg porosimetry is characterized by two peaks associated to the macroporosity and the microporous aggregates, respectively centred at 10  $\mu\text{m}$  and 0.2  $\mu\text{m}$ . We note that the pore sizes inside the microporosity are less than 1  $\mu\text{m}$  and cannot be resolved by the MicroTomography. In order to estimate the structural anisotropy of the Estailades limestone, we have performed ultrasonic P-wave measurements following Louis et al. (2004) protocol. Despite its microstructural complexity, this limestone exhibits a small velocity anisotropy (~6 %), mostly supported by a preferred pore shape orientation, as revealed by the increase of velocity anisotropy of 7 % in saturated conditions. The axis of maximum velocity is aligned with the plugging direction, z (Dautriat et al. 2007).

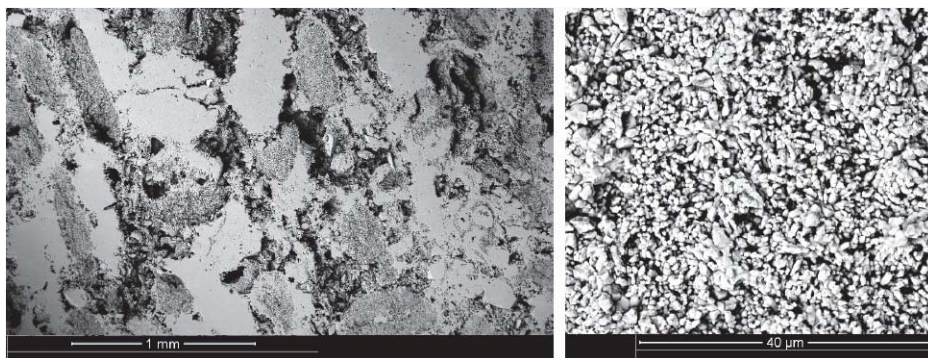


**Figure 2:** SEM images, in Backscattering Electron (BSE) mode. On the left side (a) we show the microstructure of the Estailades limestone. The macroporosity appears in black. The light and dark grey phases are respectively dense and microporous calcite aggregates. On the right side (b) we focus on the structure of the microporous calcite aggregates.

## EXPERIMENTAL RESULTS

### Validation of Experiments – Preliminary Stepwise Hydrostatic Loading

On figure 3, we present the results of a preliminary hydrostatic compression test performed in a stepwise way. This stepwise test has been conducted to integrate all the directional permeability measurements and the reduction of porosity recorded at each pressure increase step to fit accurately this complete set of measurements on a single sample. We report the evolutions of the porosity and the directional normalized permeabilities (Fig. 3a and Fig. 3c, respectively). In the range of small confining pressures, from 3 MPa to 25 MPa, the porosity and the permeabilities follow a similar linear trend, corresponding to the elastic regime. The porosity (initially at 27.5%) decreases more rapidly above 25 MPa and drops drastically to 24 % after 35 MPa. Independently of the direction measurement (axial and radial), the permeabilities also decrease strongly, to reach ~10-20% of the initial value. This pressure, referenced as the critical  $p^*$ , corresponds to an homogeneous pore collapse. This state of irreversible deformation is confirmed by the residual values of porosity (~24 %) and permeabilities (~20 mD) measured after unloading. This drastic loss of porosity and permeability can be correlated to the results of Hg porosimetry (Fig. 3d) and MCT microstructural observations (Fig. 3b) performed on the damaged sample. The Hg porosimetry reveals a shift to the left of the peak associated to the macropores from 10  $\mu\text{m}$  to 3.5  $\mu\text{m}$ , whereas the peak associated to the microporosity (0.2  $\mu\text{m}$ ) remains almost unaffected. The MCT reconstruction performed on the damaged sample shows clearly that the macroporosity is substantially affected by pore collapse, whereas the microporous aggregates do not present evidence of crushing or densification.

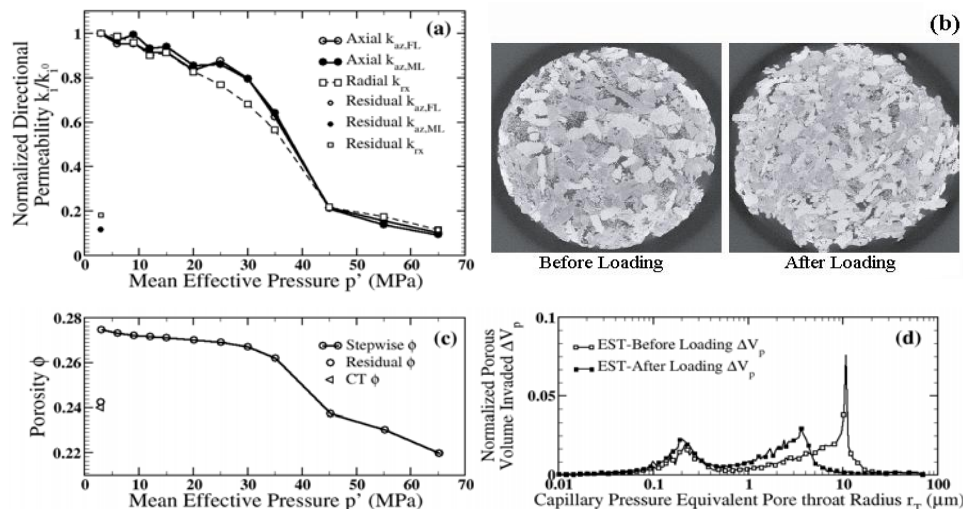


**Figure 3:** (a) Normalized directional permeabilities and (c) porosity evolutions with mean effective pressure; (b) MCT density map at 3 $\mu\text{m}$  resolution of Estailades limestone before and after stepwise hydrostatic compression; (d) Hg porosimetry from 0.01 up to 400MPa of Estailades limestone before and after the compression experiment.

### Stress Path Dependency of the Mechanical Response

On figure 4, we present the evolutions of the volumic strain, defined as  $\varepsilon_v = (\varepsilon_a + 2\varepsilon_r)$ , and the shear strain, defined as  $\varepsilon_s = 2/3(\varepsilon_a - \varepsilon_r)$ , for one of the two sets (axial k, radial k) of continuous loading experiments. According to the different applied stress paths characterized by the ratio K, we observe three deformation regimes. (1) For low stress paths ratios,  $K=0$  and  $K=0.125$ , the samples are undergoing brittle failure at a critical effective pressure  $C'$ , respectively close to 8 MPa and 13 MPa; the foregoing inelastic regime is characterized by dilatancy of the samples, occurring at 6.5 MPa and 9.6 MPa respectively. (2) When the stress paths ratio becomes greater than  $K=0.5$ , the deformation of the sample remains purely compressive beyond the elastic regime and is characterized by an important volumic strain, as observed in the stepwise hydrostatic loading (see Fig. 3), which corresponds to a pore collapse regime. (3) For intermediate stress path ratios, the samples exhibit either dilatant or compressive regime: the two samples subjected to the stress path  $K=0.25$  present an intermediate behavior; in the inelastic regime, while the radial deformation tends to be extensive, the average volumic strain is clearly compressive. In addition, we observe that the damage of the sample occurs at the highest shear stress in comparison to all the other tested samples.

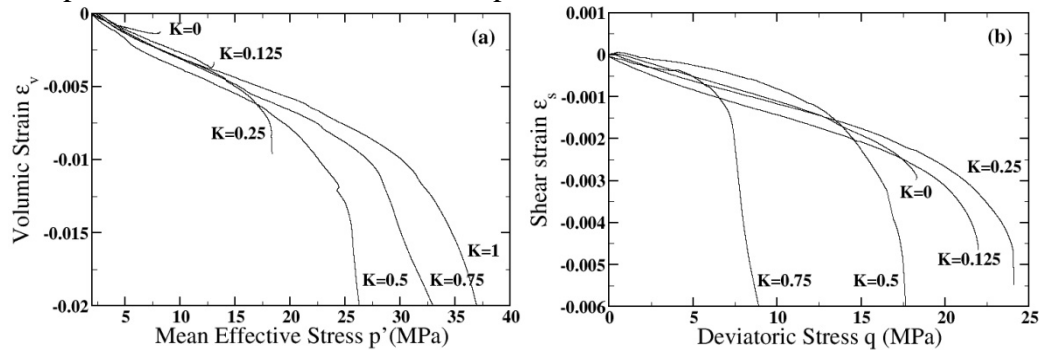


**Figure 4:** (a) Evolution of Volumic Strain with increasing Mean Effective Stress and (b) Evolution of Shear Strain with increasing Deviatoric Stress, along different stress path ratios K ranging from 0 to 1, for one of the two sets (set 1:  $k_a$ , set 2:  $k_r$ ) of the compression experiments.

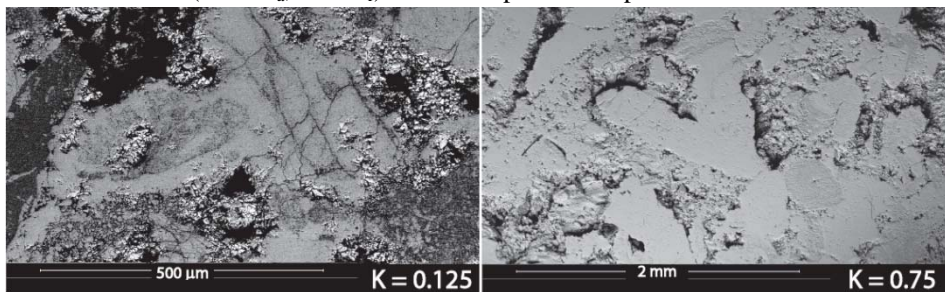


**Figure 5:** SEM images, in Back Scattering Electron (BSE) mode, of two deformed samples. On the left (a): the sample subjected to low stress path ratio  $K=0.125$  shows pervasive microfracturing of the dense aggregates. On the right (b): the sample subjected to a high stress path  $K=0.75$  shows a denser microstructure compared to the undeformed sample (see Fig. 2), which gives evidence of pore collapse.

### Inelastic Regime and Yield Envelopes

In the elastoplastic critical state model, a yield surface (cap) establishes the boundaries of the region of elastically sustainable stresses. Changes of stress within the yield surface are accompanied by purely recoverable deformations. The yield envelope can be described as an eccentric ellipse and a critical state line equated with the linear Mohr Coulomb strength envelope; its slope is best defined experimentally through a combination of drained triaxial tests at low mean effective stress (often at low confining pressure). The critical state line divides the stresses space into a zone of dilatation to the left and a zone of compression to the right. The extent of the dilation zone is delineated by the linear Mohr-Coulomb peak/fracture strength envelope and is constrained to meet the yield cap at their common point of tangency. Some authors recommend uniaxial undrained tests to constrain more efficiently this critical state line. We are not able to report the results of such undrained tests, because the monitoring of the pore pressure increase is not yet implemented in our set-up. Beyond the yield envelope, hardening parameters are required to describe how the cap evolves with strain.

Figures 6a and 6b present the criterion and method of determination of inelastic and yield stresses, used in our study. The inelastic stress is determined by the deviation from purely elastic response, such as the departure point from linearity of axial strain. The yield stress is determined either by the intersection of the tangents to the elastic and plastic responses for stress path ratio  $K \geq 0.5$  (when the plastic regime is well identified and showing a mostly linear response, as see on Fig. 6a), or directly by the peak strength, for small  $K$  leading to a brittle regime at high differential stress  $q$  (see Fig. 6b). A critical state interpretation for the Estailades Limestone is shown on figure 6c with drained  $K$ -paths represented as solid straight lines. Many authors (Baud et al. 2006) agree to conclude that the initial yield stresses at the onset of shear-enhanced compaction are in good agreement with an elliptic cap with semi-axes  $A$  and  $B$  and center at  $(C, 0)$ , represented by equation:

$$\frac{(P-C)^2}{A^2} + \frac{Q^2}{B^2} = 1,$$

It is also assumed that both the initial and subsequent yield stresses can be described by such elliptic caps. For the Estailades limestone, with such assumption, we find (see Fig.6c): (1) for the departure from elasticity, the best fit is obtained with parameters  $A=9.46$ ,  $B=13.33$  and  $C=12.02$ ; (2) for the yield cap, the best fit is obtained with the set  $A=15.73$ ,  $B=21.06$  and  $C=17.09$ . More generally, these three parameters should be functions of the volumic strain. These two inelastic limits and yield caps are shown as dashed lines and curves on figure 6c. However, owing to the limestone heterogeneity, we observe that between two samples subjected to the exact same stress path, the initiation of yield deformations may happen at fairly different stress levels. For instance, mechanisms of pore collapse activated for a stress path ratio  $K=0.75$ , occur at  $p'=34 \text{ MPa}$  for one experiment, and at  $p'=24 \text{ MPa}$  for the other. While our yield data present some scattering, the pertinence of an elliptic cap model seems reasonable. Lower and upper bounds of the

caps are reported as lighter dashed curves. Further experiments are needed to define more accurately the bounds and shape of the yield envelope. On the figure 6c, we also report the yield stress determined with an Unconfined Compressive Strength (UCS) test conducted on an axial loading bench in dry condition, in order to constrain more efficiently the brittle failure criterion (Mohr-Coulomb line). Our set-up is not well adapted for UCS tests, because to conduct permeability measurements, we apply a small confining pressure to ensure the core/sleeve sealing. Uniaxial Compression Test (imposed zero radial strain), more representative of reservoir loading path, will be performed as well, when the servo-control of radial strain by confining pressure will be operational.

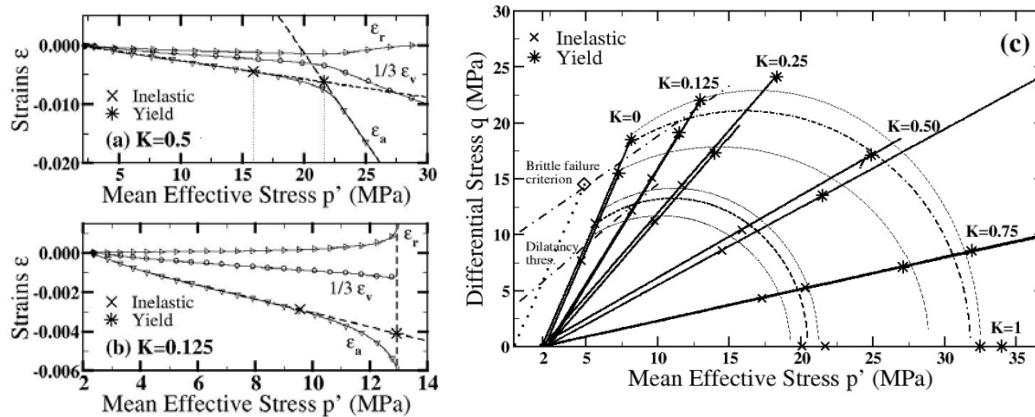


**Figure 6:** Examples of determination of Inelastic (cross) and Yield (star) stresses from stress-strain curves, on Estailades samples subjected to loading with stress path ratio (a)  $K=0.5$  and (b)  $K=0.125$ . (c) Inelastic and Yield envelopes determined from the compression experiments with stress path ratios from  $K=0$  to  $K=1$ , and from an additional UCS test (diamond symbol). Eccentric elliptic caps in the compaction regime (right) and Mohr-Coulomb Line in the dilatation regime (left).

### Directional permeabilities evolutions

Figure 7 presents the evolutions of axial and radial normalized permeabilities  $k/k_0$  ( $k_0$  at  $p_0=30\text{bar}$ ) measured during continuous loading versus the mean effective stress  $p'$  for the different stress paths. The axial permeability measurements were performed up to the initiation of the fracture or pore collapse, after which the loading is stopped and the stresses decreased back to the initial hydrostatic stress. The radial permeability measurements were measured up to the maximum axial pressure of  $65\text{MPa}$ . For both axial and radial permeabilities, in the regime of elastic deformation, we observe a linear evolution of permeability with the mean stress. Taking into account, the fluctuations of permeability at low mean stress (mainly due to the sensitivity of the pressure differential sensor), the reduction rate of axial permeability seems to increase slightly as the stress path ratio decreases (see Fig. 7a). Also, this permeability reduction rate is more pronounced for radial permeability (direction transverse to the maximal axial stress) (see Fig. 7b) even for  $K=1$ . This could be related to a greater influence of the initial pre-existing microstructural anisotropy during elastic compaction. Once the inelastic threshold is reached, the

permeability reduction deviates from linearity and diverges in the vicinity of the yield stress. For radial permeability (see Fig. 7b) measured beyond the critical pressure of pore collapse (stress path ratio greater than  $K \geq 0.25$ ), transition from elastic to plastic deformation response is clearly marked. As the rock stiffens at high mean pressure, permeability stabilizes and tends to follow again a linear behaviour. The same directional permeabilities data can also be plotted versus the shear stress  $q$  (see Fig. 7c and Fig. 7d) to identify the role of shear mechanisms. We observe that the resistance of the rock to shear stress is maximum for low to intermediate stress path ratios  $0.125 < K < 0.25$ . As a consequence, the linear decrease of permeability holds until shear stress  $q \sim 15 \text{ MPa}$  to  $20 \text{ MPa}$  in this intermediate regime. For small  $K$ , a lower shear stress generates fracture leading potentially to a permeability increase, whereas for large  $K$ , plastic compaction develops also at lower shear stress.

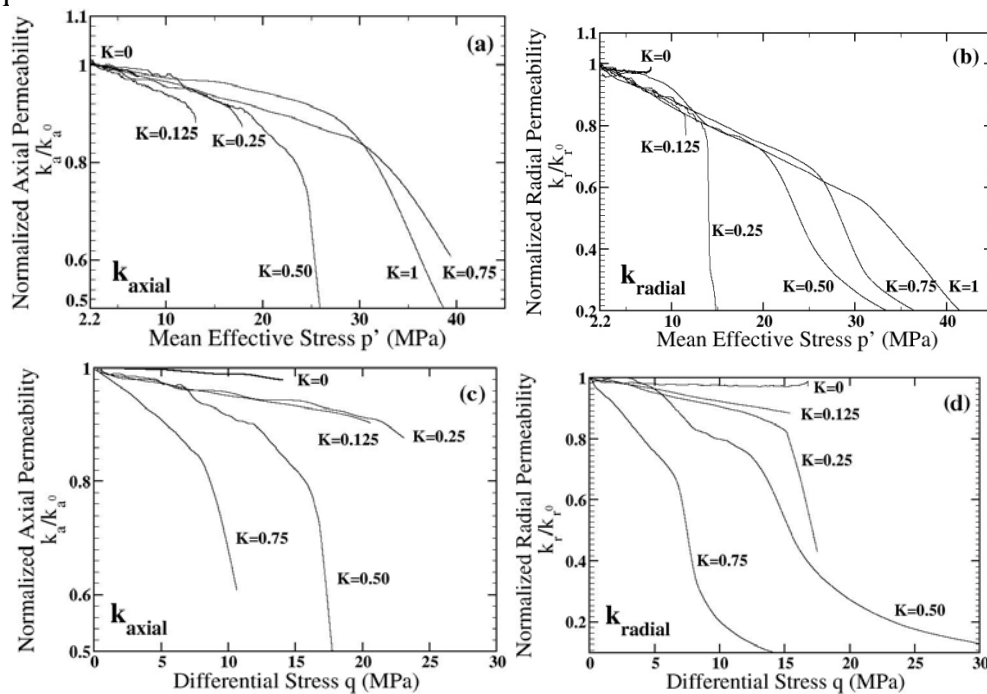


**Figure 7:** Normalized axial and radial permeabilities evolutions with Mean Effective Stress  $p'$  (respectively a and b), and with Differential Stress (respectively c and d) for stress path ratios ranging from  $K=0$  to  $K=1$ .

The data of figures 7 have been transposed in the  $(p',q)$  stress space (see Fig. 8); the axial and radial isopermeabilities contours were constructed using a linear interpolation function. A suitable window averaging has been applied to the data to limit the fluctuation effects discussed previously, resulting in smoothed  $k$ -surfaces. Each contour corresponds to a permeability reduction of 5 %. We also report on this figure the stress paths and the inelastic and yield envelopes. Permeabilities are mapped on both dilatant and compactive

regions. While, for the axial permeability (see Fig. 8a), the compression has been stopped at the yield stress, for the radial permeability, the compression was pushed above, and the interpolation becomes possible for higher mean effective stress.

In the near-elastic regime, radial permeability decreases faster than axial permeability. For stress path  $K > 0.25$ , the iso-permeability contours get closer when the inelastic yield is reached, and remain quite congruent with the yield cap. Beyond the yield cap, the rate of radial permeability decrease slows down, due to sample hardening. For stress path  $K < 0.25$ , at high shear stress, the iso-permeability contours tend to deviate from verticality (control of effective mean pressure) to bend to the left following the inelastic and yield lines. Crawford and Yale (2002) observed similar results on 'high porosity/high permeability' carbonates. The isopermeability contours are close to verticality in the near elastic regime. The permeability response appears to be essentially controlled by the mean effective pressure, meaning that the hydrostatic part of the stress tensor is primarily responsible for the permeability reduction. The higher radial permeability decrease could be induced by the initial structural anisotropy of the samples. The deviation of isopermeability contours observed in the yield cap vicinity could be related to a more important contribution of shear mechanisms in this deformation regime. As observed by Shafer et al. (2008), stress dependency of permeabilities may differ between constant pore pressure stress paths, investigated in this study, and pore pressure depletion tests.

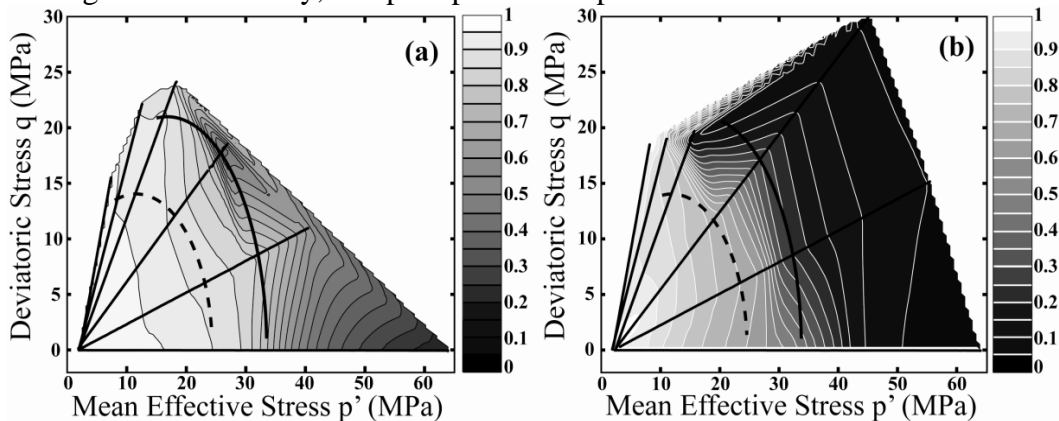


**Figure 8:** Axial (a) and radial (b) isopermeability contours spaced of an equivalent permeability reduction of 5%, transposed into the  $(p', q)$  plane. Straight lines represent the different slopes of the applied stress paths, and dashed lines are the inelastic and yield cap.

## CONCLUSIONS

We have measured the deformation and the evolution of axial and radial permeabilities, while running continuous triaxial compression experiments on carbonate rock characterized by bimodal porosity, following different stress paths with ratios varying from  $K=0$  to  $K=1$ . We have been able to measure permeabilities in all directions, not only in the elastic regime of deformation, but also after the critical pressure inducing important microstructural changes corresponding either to shear localization or to homogeneous pore collapse.

Microstructural analysis revealed that for low K, dense calcite aggregates were microfractured, whereas for high K, pore collapse acts as a diffuse mechanism affecting essentially the macroporosity. On our experimental data sets, we have applied a methodology for the construction of the inelastic and yield caps in the (p',q) diagram. In addition, we have mapped the axial and radial permeability responses as isocontours in the (p',q) stress space. For large K ratios, in the near elastic regime, we observe that permeability evolutions are mostly related to the hydrostatic component of the applied stress field. The more pronounced reduction of radial permeability remains to be investigated in the continuation of this work; it may be related to the initial microstructural anisotropy of this Estailades limestone. For small K ratios, at high stress, the directional permeabilities are mostly influenced by the shear stress. Such petrophysical data of directional permeabilities alteration mapped in the (p',q) stress space, could be introduced in coupled reservoir/geomechanic simulation tools to improve production management of stress sensitive reservoirs, due to strong interactions between stress-strain states, rock fabrics and associated flow properties.

## REFERENCES

- Bai M., Meng F., Roegiers J.C. and Green S., "Improved Determination of Stress-Dependent Permeability for Anisotropic Formations", *SPE/ISRM*, **78188**, 2002.
- Baud P., Vajdova V. and Wong T.F., "Shear-Enhanced Compaction and Strain Localization: Inelastic Deformation and Constitutive Modelling of four Porous Sandstones", *J. Geophys. Res.*, **111**, 2006.
- Crawford B.R. and Yale D.P., "Constitutive Modelling of Deformation and Permeability: Relationships between Critical State and Micromechanics", *SPE/ISRM*, **78189**, 2002.
- Dautriat J., Gland N., Dimanov A. and Raphanel J.L., "Axial and Radial Permeability Evolutions of Compressed Sandstones: End Effects and Shear Band Induced Permeability Anisotropy", *Pure & Appl. Geophys.*, **submitted**, 2008.
- Dautriat J., Gland N., Youssef S., Rosenberg E. and Bekri S., "Stress-Dependent Permeabilities of Sandstones and Carbonates: Compression Experiments and Pore Network Modelings", *SPE/ATCE*, **110455**, 1-22,2007.
- Heiland J. and Raab S., "Experimental Investigation of the Influence of Differential Stress on Permeability of a Lower Permian Sandstone Deformed in the Brittle Deformation Field", *Phys. Chem. Earth (A)*, **26**, 33-38, 2001.
- Jones J.P. and Mathiesen, E., "Pore Pressure Change and Compaction in North Sea Chalk Hydrocarbon Reservoirs", *Int. J. Rock Mech. Min. Sci.*, **30**, 1205-1208, 1993.
- Louis L., Robion P. and David C., "A Single Method for the Inversion of Anisotropic Data Sets with Application to Structural Studies", *J. Struct. Geol.*, **26**, 2065-2072, 2004
- Rhett D. W. and Teufel L. W.: "Stress Path Dependence of Matrix Permeability of North Sea Sandstone Reservoir Rock", *Proc. 33<sup>rd</sup> US Symp. Rock Mechanics*, 345-355, 1992.
- Schutjens P.M.T.M. and De Ruig H., "The Influence of Stress Path on Compressibility and Permeability of an Overpressurized Reservoir Sandstone.", *Phys. Chem. Earth (A)*, **22**, 97-103, 1997.
- Shafer J.L., Boitnott G.N. and Ewy R.T., "Effective Stress Laws for Petrophysical Rock Properties", *Proc. 49<sup>th</sup> SPWLA Annual Symp.*, 1-15, 2008.
- Yale D.P. and Crawford B., "Plasticity and Permeability in Carbonates: Dependence on Stress Path and Porosity", *SPE/ISRM*, **47582**, 485-494, 1998.
- Yale D.P., "Coupled Geomechanics - Fluid Flow Modeling: Effects of Pasticity and Permeability Alteration", *SPE/ISRM*, **78202**, 1-10, 2002.